Contents lists available at ScienceDirect

Thermal Science and Engineering Progress

journal homepage: www.sciencedirect.com/journal/thermal-science-and-engineering-progress

# Fused filament fabrication of phase change materials in high density polyethylene with expanded graphite for shape-stabilization and thermal conductivity enhancement

Sereno Sacchet [a,*], Mirko Coser [a], Francesco Valentini [a], Maurizio Grigiante [b], Riccardo Po [c], Luca Fambri [a,*]

[a] Department of Industrial Engineering and INSTM Research Unit, University of Trento, 38123, Italy
[b] Department of Civil, Environmental and Mechanical Engineering, University of Trento 38123 Trento, Italy
[c] Renewable, New Energies and Materials Science Research Center, "Istituto Guido Donegani", Eni S.p.A., 28100 Novara, Italy

ARTICLE INFO

*Keywords:*
Additive manufacturing
Passive cooling
Thermal management
Thermal energy storage
PCM
Expanded graphite
HDPE
Fused filament fabrication

ABSTRACT

Organic Phase Change Materials (PCMs) are essential for passive cooling, yet their poor shape stability and low thermal conductivity limit their integration into advanced manufacturing techniques. Addressing this, we report a novel, high-performance functional composite filament developed for the first time for Additive Manufacturing (AM) via Fused Filament Fabrication (FFF). The composite leverages a non-microencapsulated PCM (fatty acid mixture, $T_m = 55$ °C) confined within a high-density polyethylene (HDPE) matrix, chosen for its low processing temperature (140–160 °C) to prevent PCM degradation. Expanded graphite (EG) was preliminarily vacuum-impregnated with the PCM and subsequently melt-compounded with HDPE, serving as a multifunctional filler to enhance both thermal transport and structural stability. The resulting filament was successfully processed into 3D-printed geometries, achieving a high PCM loading of 36 wt% and a melting enthalpy of 70 J/g. Comprehensive analysis revealed a significantly enhanced thermal conductivity, reaching 0.8 W/m·K, and a Figure of Merit of $0.71 \cdot 10^4$ W/($m^2 \cdot K^{0.5} \cdot s^{0.5}$), effectively balancing thermal response with energy density. Crucially, the synergistic architecture formed by the HDPE matrix and the EG functional filler ensures exceptional PCM shape stability and robust leakage resistance, while retaining superior mechanical integrity across the entire temperature range of the phase transition. This work demonstrates a viable and scalable manufacturing route for producing multifunctional, high-loading PCM composites with exceptional potential for thermal management in demanding applications like battery and electronic cooling.

## 1. Introduction

The integration of organic Phase Change Materials (PCMs) into additive manufacturing (AM) has emerged as a promising strategy for enhancing thermal management and thermal energy storage (TES) capabilities in a wide range of applications, including energy-efficient buildings and electronics cooling. PCMs exhibit the ability to absorb, store, and release latent heat during phase transitions, making them highly effective for the thermal management of devices such as photovoltaic (PV) panels and batteries. However, their practical implementation is often hindered by challenges related to material encapsulation, structural stability, and thermal degradation. Consequently, there is a growing interest in developing advanced fabrication techniques that enable the efficient incorporation of PCMs into functional structures while maintaining their thermal and chemical stability [1].

Within the realm of polymer-based AM, several techniques have been explored for the integration of PCMs into matrices, with particular interest in thermoplastic and thermosetting polymers. Stereolithography (SLA) [2,3] and Digital Light Processing (DLP) [4–6] have been utilized to create PCM-embedded photopolymer composites with high precision and complex geometries, although the challenge of PCM leakage and phase separation during thermal cycling remains a concern, accompanied by the recurring loss of lateral resolution and the inability to print thick layers. Selective Laser Melting (SLM) [7] has been investigated for incorporating PCMs in metallic structures, offering tunable porosity and structural integrity. Nevertheless, ensuring homogeneous PCM dispersion and mitigating thermal degradation during the sintering process present significant challenges. Additionally, Direct Ink Writing (DIW) [8,9] has demonstrated potential for extruding PCM-infused polymeric pastes, providing control over material deposition and homogeneous PCM distribution within the printed structure. However, the control of the viscosity is quite difficult when trying to obtain the expected resolutions and maintaining post-printing mechanical integrity is a critical concern. Finally, Fused Jet Deposition (FJD) was exploited for printing PCM flexible electronic packaging. However, this technique is suitable only for obtaining thin structures [10]. While these techniques offer promising pathways for PCM integration in complex-shape composites, many of them face inherent difficulties in balancing thermal performance, mechanical stability, and long-term PCM retention. Furthermore, the matrices are often thermoset polymers, hence these solutions are little sustainable from a circular economy point of view, because it is impossible to recycle them.

Fused Filament Fabrication (FFF) is a promising alternative among AM techniques for the fabrication of PCM-based composite structures. FFF presents advantages such as accessibility, cost-effectiveness, and the ability to produce complex geometries with tunable thermal properties; moreover, unlike other polymer-based AM techniques, FFF enables scalable production and straightforward material handling [11]. Additionally, the layer-by-layer deposition process enables precise control over the distribution of PCMs within printed structures, offering opportunities to optimize heat absorption and release while maintaining mechanical stability. Despite these advantages, the successful integration of PCMs into thermoplastic filaments for FFF remains a considerable challenge. The inherent immiscibility between many thermoplastics and PCMs can lead to phase separation, material heterogeneity, and poor interfacial adhesion, all of which can compromise both printability and long-term functionality. Furthermore, the thermal processing conditions of FFF, including high extrusion temperatures and repeated thermal cycling, pose a risk of PCM degradation, leakage, or evaporation, potentially diminishing the thermal storage capacity of the material. Achieving a balance between sufficient PCM loading for effective latent heat storage and maintaining the mechanical integrity of filament and printed part is another critical obstacle. In addition to material-related issues, processing challenges further complicate the feasibility of PCM-loaded filaments. The presence of PCMs can alter the rheological behaviour of the filament, affecting extrusion stability, layer adhesion, and print resolution. While these challenges highlight the complexities associated with PCM integration in FFF, they also underscore the need for innovative material formulations, processing optimizations, and structural design strategies [1].

The first pioneering results were probably obtained by Rigotti *et al.*, who successfully incorporated 50 wt% of micro-encapsulated PCM (melting temperature of 6 °C) into thermoplastic polyurethane (TPU), reaching composites with 70 J/g of melting enthalpy [12,13]. However, TPU must be processed at temperatures of 180–200 °C, exposing PCM to thermal degradation due to the long permanence time of the blend in the compounder and extruder. The same problem affects the results of Singh *et al*, who exceeded 200 °C in the processing of polyamide [14]. Salgado-Pizarro *et al.* obtained via Material Extrusion Granulate a composite incorporating PCM into a polycaprolactone (PCL) matrix, whose main limitation is the maximum working temperature below 60 °C [15]. Recently, Foster *et al.* processed at 160–200 °C PCL and TPU blends with 60 wt% of microencapsulated-PCM (melting temperature of 6 °C), combining thermoplastic polymer ratios to tune the matrix properties [16]. However, the need to preserve PCM integrity suggests moving towards lower processing temperature. In addition, many of these processes require the use of micro-encapsulated PCM, with the disadvantage of cost increase and heat absorption reduction.

High Density Polyethylene (HDPE) emerges as a compelling candidate for the fabrication of PCM-based composites via FFF, offering several advantages that address some of the key challenges associated with PCM integration, such as good miscibility between matrix and PCM. As a semicrystalline thermoplastic, HDPE possesses a relatively low melting temperature (130–140 °C), which is advantageous for processing PCM-based compounds, as it reduces the risk of thermal degradation during compounding, extrusion, and printing [17]. This characteristic makes HDPE particularly suitable for maintaining the stability of temperature-sensitive PCMs while ensuring the integrity of the filament and printed structures. Other key benefits of HDPE are its excellent chemical resistance and low moisture absorption, which contribute to the long-term stability of PCM-filled composites. From a mechanical perspective, HDPE exhibits a favourable combination of flexibility and toughness, which can mitigate brittleness problems caused by the presence of PCMs and improve the mechanical properties of printed components. Additionally, its relatively low density enables the production of lightweight thermal storage components. Freeman *et al.* successfully printed blends of HDPE and non-microencapsulated PCM [18,19]. However, the absence of a shell for the PCM confinement prevents the obtaining of high PCM loadings, and leakage remains an issue. Furthermore, the low thermal conductivity remains a limiting factor for applications involving heat transfer in all these works.

High thermal conductivity composites were obtained by Nofal *et al.*, who built an expanded graphite (EG) matrix containing a paraffin wax via selective self-binding laser sintering [20,21]. EG was also combined with HDPE and carbon fibres by Cao *et al.*, who additionally improved thermal conductivity through an aluminium honeycomb structure [22]. These are smart solutions in improving thermal conductivity, but the former must sacrifice the benefits of HDPE as a ductile matrix, while the latter loses the benefits of the complex geometries obtainable via FFF.

In an effort to balance all these requirements, this study focuses on a PCM with a melting temperature of 55 °C and aims to combine complex-shaped composites made by AM, achieving good mechanical properties through the presence of HDPE, and improving thermal conductivity of PCM with EG, which acts as a conductive filler and shape stabilizer. We propose first stabilizing the PCM within an EG matrix, obtained via a vacuum impregnation process [23–25], resulting in a highly conductive PCM-based powder instead of the typical polymer shell of microcapsules. The powdery graphite containing the PCM is then incorporated into HDPE, serving as a printable matrix for the composite. This approach improves upon a previous triple-phase material produced through hot compression moulding [25], intending to create composites with enhanced thermal conductivity through AM.

The goal of this study is to develop a high-performance composite material by transitioning from traditional hot compression molding to a flexible additive manufacturing approach. Specifically, this work focuses on optimizing three critical conditions: (i) thermal management performance; (ii) enhanced thermal conductivity; (iii) production flexibility via AM.

## 2. Experimental part

### 2.1. Materials

The selection of the Phase Change Material (PCM) was driven by previous investigations into the interaction between organic PCMs and Expanded Graphite (EG) [23–25]. A fatty acid mixture was chosen specifically for its superior leakage resistance compared to paraffins when impregnated into EG [24]. As a proof-of-concept for this manufacturing route, a palmitic and stearic acid mixture (SA), commercially named "Fatty Acids C16-18" (Carlo Erba Reagents, Val De Ruil, France), was selected, featuring a melting point of 55 °C.

The first shape stabilization was achieved using a commercial EG, "SIGRAFLEX® Highly Conductive Expanded Graphite Powder", (SGL Carbon GmbH, Meitingen, Germany), characterized by a tapped density of 25 g/L at room temperature.

The thermoplastic matrix enabling filament production, is High Density Polyethylene (HDPE), specifically Plastene® AD25 (Poliplast S.

* Corresponding authors.
*E-mail addresses:* sereno.sacchet@unitn.it (S. Sacchet), luca.fambri@unitn.it (L. Fambri).

https://doi.org/10.1016/j.tsep.2026.104596
Received 25 November 2025; Received in revised form 27 January 2026; Accepted 16 February 2026
Available online 18 February 2026

p.A., Casnigo, Italy). It was supplied as a fine powder with a density of 0.955 g/cm$^3$ and a melt flow index (MFI) of 25 g/10 min (at 190 °C, 2.16 kg).

### 2.2. Sample preparation

The composite fabrication process consists of a sequence of well-known preparative steps, schematically represented in Fig. 1.

The formulation was developed through a two-stage optimization process to balance thermal performance with AM requirements. First, the PCM-to-EG ratio was fixed at 100:14, a value previously identified as the optimum for achieving shape-stabilization and a high Figure of Merit (FoM) [23].

While initial attempts utilized a 70 wt% of PCM/EG loading (PE-70SA/EG14) based on hot-compression protocols [25], this composition exhibited excessively low melt viscosity. This high MFI precluded the extrusion of a calibrated filament, though it remained suitable for bulk objects. To adapt the material for AM, it was necessary to reduce the PCM content and complementary increase the HDPE fraction to 50 wt%. This adjustment effectively reduced the MFI to a range compatible to filament production. The final optimized composition (PE-50SA/EG14) is reported in Table 1, alongside the comparative samples present in this work.

The preparation began by vacuum impregnating the EG with the PCM to ensure initial shape stabilization. Specifically, 100 g of SA and 14 g of EG were weighted and hand-mixed when inserted in a 1 L flask. The mixing process continued in vacuum conditions (50–60 mbar) for 10 min at room temperature using a rotavapor at 20 rpm. This intermediate step was crucial for removing air within the EG structure before impregnation while the PCM was in the solid state. If not sufficiently removed, residual air within the EG structure would generate voids, diminishing impregnation efficiency and structural integrity. Subsequently, the water bath was heated to 90 °C, allowing the PCM melting and its gradual infiltration into the EG interconnected porosity. Following PCM complete melting, rotation in the heated bath was maintained for 30 min to ensure a homogeneous impregnation of the molten SA into the EG, where it remained entrapped within the interlayer spacing of the carbon planes via capillary forces. The resulting product (PCM/EG) was a dry powder, denominated SA/EG14 [23,24].

The second shape stabilization consisted of dispersing the EG/PCM powder into the HDPE matrix via melt compounding using a Thermo Haake Rheomix 600 (Thermo Fisher Scientific, USA) equipped with counter-rotating rotors. The chamber was set at 135 °C, and the rotor speed was set at 50 rpm. Initially, the HDPE was processed for 5 min to ensure complete melting and homogenization. The PCM/EG powder was then introduced gradually to facilitate proper incorporation without PCM leakage from the EG porosity. After compounding for 7 min to ensure a homogenous distribution of phases, the blend was cooled and machined using an RN 166/1 granulator (3 mm sieve). The resulting millimetric pellets were used to feed the extruder hopper for the filament production.

**Table 1**
Nominal composition of the novel additively manufactured composite (PE-50SA/EG14) and the reference materials, including neat HDPE and the previously reported high-loading formulation (PE-70SA/EG14 [25]).

| Sample code | HDPE [wt. %] | SA [wt. %] | EG [wt. %] | MFI* [g/10 min] | Process |
|---|---|---|---|---|---|
| HDPE | 100 | 0 | 0 | 13.7 ± 0.6 | Hot compression moulding |
| PE-70SA/EG14 [25] | 30 | 61.4 | 8.6 | 309 ± 23 | Hot compression moulding |
| PE-50SA/EG14 | 50 | 43.9 | 6.1 | 118 ± 11 | Additive manufacturing |

*Melt Flow Index at 160 °C and applying 2.16 kg.

The filament was realized using a Thermo Haake Rheomex (Thermo Fisher Scientific, USA) twin-screw extruder (D = 16 mm, L/D = 25) at 5 rpm, with a temperature profile ranging from 60 °C to 140 °C, according to Fig. 1. To meet the rigorous requirements of FFF, the material was extruded through a 1.8 mm nozzle and immediately subjected to abundant air cooling. This forced crystallization of the HDPE matrix allowed the filament to be drawn to a standardized diameter of 1.75 ± 0.10 mm, obtaining a density of 1.04 ± 0.03 g/cm$^3$ and a titer of 2500 ± 200 tex, as documented in Fig. 2.

The final stage involved the 3D printing of the as-produced filament via Fused Filament Fabrication (FFF) using a Creality Ender 3 V2 3D printer (Shenzen, China). Slicing was performed with Ultimaker Cura software (https://ultimaker.com/software/ultimaker-cura/). A printing temperature of 160 °C was adopted, and to address the inherent adhesion challenges of the HDPE matrix, an auxiliary HDPE build plate was glued to the original glass bed heated at 45 °C.

To further ensure a robust bond, the nozzle-to-plate distance for the

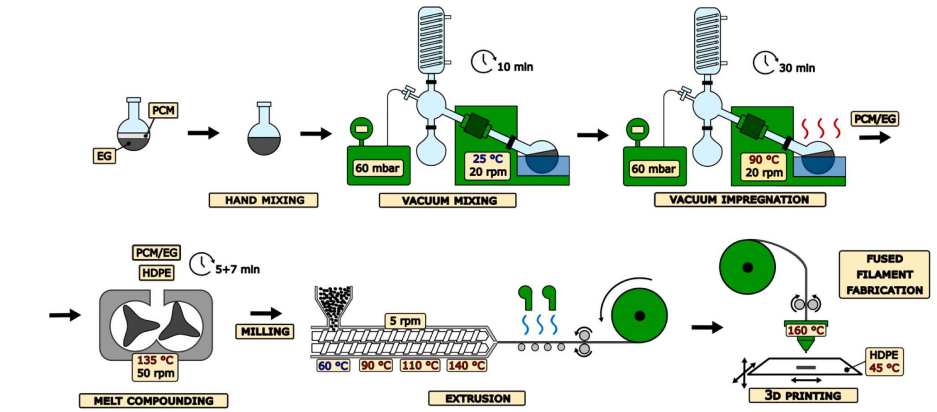


**Fig. 1.** Schematic flow chart of the composite preparation process, illustrating the two-stage stabilization strategy: (i) vacuum impregnation of the PCM into EG, and (ii) melt compounding of the resulting SA/EG powder with the HDPE matrix followed by filament extrusion for 3D printing.





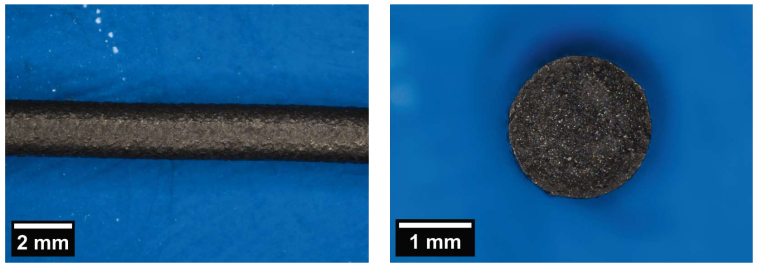


**Fig. 2.** Optical observation of the produced filament: a) Side view; b) cross-section.

first layer was calibrated at 0.5 mm, which promoted localized surface melting between the HDPE and printed material. To facilitate successful specimen removal, a two-layer raft with air gap of 0.1 mm was employed (Fig. A1). Printing parameters included a layer height of 0.2 mm, a line width of 0.4 mm, and a wall line count of 2, utilizing an Infill/Top/Bottom concentric pattern. The specific dimensions and processing parameters for the resulting specimens (modelled in Fig. 3) are summarized in Table 2.

### 2.3. Experimental methodologies

The morphological features of the produced samples were observed by optical microscopy using a Nikon MSZ25 microscope (Nikon Instrument, Tokyo, Japan). To evaluate the internal structure and phase distribution at higher magnifications, Scanning Electron Microscopy (SEM) was performed on fracture surfaces by using a Zeiss Supra field emission scanning electron microscope (Carl Zeiss, Oberkochen, Germany). The secondary electron signal was obtained by applying an acceleration voltage of 2.5 kV and covering the sample surfaces with a thin layer of Pt-Pd.

The apparent density of the neat components (SA, and HDPE), and the composite material was determined at 20 °C with an Ultrapyc 5000 helium pycnometer (Anton Paar, Austria) equipped with a 4.5 cm$^3$ chamber, performing 30 measurements for each sample. Based on these experimental values, the internal void fraction ($\vartheta_V$) within the PE-50SA/EG14 composite was calculated according to Equation (1).

$$\vartheta_V = \frac{\rho_{th} - \rho_{exp}}{\rho_{th}} \bullet 100 \quad (1)$$

where $\rho_{exp}$ represents the experimental density of the composite measured via helium pycnometry, while $\rho_{th}$ denotes the theoretical density of the composite material, calculated based on the effective composition determined from TGA, and the density of the single constituents. For these calculations, the experimental pycnometer density of SA and HDPE (as reported in Table 3), along with a theoretical density of 2.26 g/cm$^3$ for the EG [23].

The thermal mass evolution of the material was investigated via thermo-gravimetric analysis (TGA) using a Mettler TG50 thermobalance (Mettler-Toledo, Greifensee, Switzerland). Specimens of approximatively 10 mg were placed in an alumina crucible and heated from 30 °C to 700 °C at a constant heating rate of 10 °C/min under a nitrogen flux of 100 mL/min. The degradation behaviour was characterized through the analysis of both TGA and derivative thermogravimetric (DTGA) curves. This allowed for the quantification of the constituent phases by evaluating selected results: the temperature associated to 5 wt % of mass loss ($T_{5\%}$), the temperature associated to the maximum degradation rate ($T_{peak}$), the residual mass at 425 °C ($m_{425}$), and the residual mass at 700 °C ($m_{700}$).

The ability of the 3D-printed composite to retain the molten PCM was quantified through a forced leakage test conducted at 70 °C. This temperature was specifically chosen to be significantly above the melting point of the PCM to simulate extreme operating conditions. The test involved monitoring the cumulative mass loss over a duration of 150 h. For this analysis, three disks of diameter 12.5 mm and thickness 2.4 mm were placed into an oven by leaving them on a porous filter paper (Extra Rapida – Perfecte 2, provided by Gruppo Cordenons S.p.A., characterized by grammage of 90 g/m$^2$ and thickness 196 μm) to favour the PCM extraction. The leakage performance was quantified as the percentage of mass loss relative to the initial mass, with all loss attributed to PCM leakage. Results are reported as mean value ± standard deviation.

Differential Scanning Calorimetry (DSC) was performed to establish the phase transition temperatures and enthalpies using a Mettler DSC 5+ calorimeter (Mettler-Toledo, Greifensee, Switzerland). Specimens of approximatively 10 mg were encapsulated in 40 μL aluminum crucibles

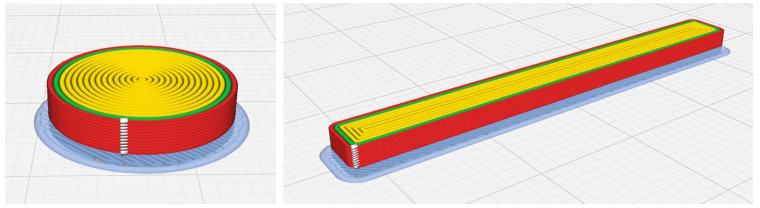


**Fig. 3.** Digital models and slicing configurations of the 3D-printed specimens (designed by Ultimaker Cura): a) Disk; b) Bar 1.

**Table 2**
Dimensional specifications and FFF processing parameters of the realized specimens.

| Sample | Basal area [mm$^2$] | Thickness [mm] | Filaments in a layer | Total layers | Total time with/without raft [min] | Layer deposition time [sec] | Volume [mm$^3$] | Volume deposition time [mm$^3$/sec] | Analysis |
|---|---|---|---|---|---|---|---|---|---|
| Disk | π 12.7$^2$ / 4 | 2.4 | 32 | 12 | 3:23 / 2:46 | 13.8 | 317 | 1.91 | Thermal Diffusivity, Leakage test |
| Bar 1 | 45 x 5 | 2 | 12 | 10 | 4:18 / 3:15 | 19.5 | 450 | 2.31 | Flexural test |
| Bar 2 | 40 x 4 | 2 | 10 | 10 | 3:16 / 2:28 | 14.8 | 320 | 2.16 | DMA, Vicat |

**Table 3**
Experimental density of the neat materials and the composite at 20 °C, determined via helium pycnometry.

| Sample | $\rho_{pic}$ (g/cm$^3$) |
|---|---|
| SA | 0.9982 ± 0.0003 |
| HDPE | 0.9603 ± 0.0001 |
| PE-50SA/EG14 | 1.0047 ± 0.0002 |

with pierced lid and tested under a nitrogen flux of 100 mL/min. To simulate practical operating conditions after resetting the thermal history of the material, a thermal cycle consisting of an initial heating scan, a cooling ramp, and a second heating scan was performed. The analysis was conducted within a temperature range 35–65 °C at a constant rate of ± 1 °C/min. The peak transition temperature for the first heating ($T_{m1}$), cooling ($T_c$), and second heating ($T_{m2}$), along with their corresponding enthalpies ($\Delta H_{m1}$, $\Delta H_c$, and $\Delta H_{m1}$) were evaluated from the resulting thermograms. To assess the thermal performance of the composite material relative to the neat PCM, the effective PCM content ($PCM_{m2}^{eff}$), and the efficiency of melting ($\eta_{m2}$), were calculated from the second heating scan, according to Equations (2) and (3).

$$PCM_{m2}^{eff} = \frac{\Delta H_{m2}}{\Delta H_{m2,PCM}} \bullet 100 \quad (2)$$

$$\eta_{m2} = \frac{\Delta H_{m2}}{\Delta H_{m2,PCM} \bullet W_{PCM}} \bullet 100 \quad (3)$$

where $\Delta H_{m2,PCM}$ represents the specific enthalpy of the neat PCM during the second heating scan, and $W_{PCM}$ denotes the weight fraction of the PCM. Additionally, to assess the long-term cyclic reliability of the 3D-printed composite, 150 consecutive heating and cooling cycles were performed using the DSC parameters previously established. For representative cycles, the phase transition temperatures and enthalpies were recorded. Specifically, the crystallization enthalpy associated with the secondary peak was independently quantified and denoted as $\Delta H_{c,FREE}$. This peak is attributed to a fraction of the PCM that, while still effectively confined and stabilized within the HDPE/EG network, is subject to lower interfacial constraint compared to the PCM in the primary peak. This approach allows for the monitoring of the energy repartitioning between these two confined states over repeated thermal loading.

The bulk density profile as a function of temperature was constructed by incorporating the Coefficient of Volumetric Expansion (*CVTE*), determined by combining different techniques in linearized temperature intervals. Further information is available in the supplementary material (Equations S1 and S2, Fig. S1).

The specific heat capacity ($c_p$) was determined according to the ASTM E1269-11 standard [26] using a Mettler DSC 5+ calorimeter (Mettler-Toledo, Greifensee, Switzerland). The experimental procedure consists in a comparative method using a sapphire reference. The analysis was conducted from 10 °C to 95 °C at a constant scanning rate of 1 °C/min. The specific heat capacity was evaluated at 5 °C increment between 15 °C and 90 °C. Three specimens for each sample (mass approximatively 10 mg) were analysed to ensure reproducibility, and the results were reported as mean value ± standard deviation.

Thermal diffusivity ($\alpha$) was evaluated using a Neztsch LFA 446 Laser Flash Analyzer (Selb, Germany). The PE-50SA/EG14 specimens were disks of diameter 12.7 mm and thickness 2.4 mm, with ground faces to obtain flat and perpendicular surfaces. The SA thermal diffusivity was determined by using a sample holder for low-viscosity liquid, utilizing two stainless steel cover plates. Measurements were conducted at 5 °C increments from 15 °C to 90 °C. To ensure statistical precision, three specimens for each sample were tested. The results were reported as mean value ± standard deviation calculated considering the error propagation theory, accounting for the variability across multiple shots and specimens.

Thermal conductivity ($\lambda$) was subsequently determined as the product of the previously determined thermophysical properties according to Equation (4).

$$\lambda = \alpha \bullet \rho \bullet c_p \quad (4)$$

The calculation was performed at 5 °C intervals, from 15 °C to 90 °C. The uncertainty of the thermal conductivity values was rigorously estimated using error propagation theory, incorporating the experimental uncertainties of density, specific heat, and diffusivity.

To identify the optimal trade-off between thermal conductivity enhancement and latent heat storage capacity, the cooling capacity Figure of Merit (FoM) was determined according to Equation (5)

$$FoM = \sqrt{\Delta H_m^* \cdot \lambda} \quad (5)$$

In this expression $\Delta H_m^*$ is the volumetric latent heat of melting, calculated as the product of the mass-based enthalpy and the bulk density according to Equation (6), as presented and discussed by Shamberger [27].

$$\Delta H_m^* = \Delta H_m \bullet \rho \quad (6)$$

This metric serves as a comprehensive indicator of the material ability to simultaneously absorb thermal energy and dissipate it efficiently, allowing for a quantitative comparison between different systems.

The dynamomechanical and mechanical properties were evaluated both below and above the phase transition temperature of the PCM to make assumptions on the final applications of the material.

Dynamic Mechanical Analysis (DMA) was performed using a TA Instruments DMA Q800 machine (TA Instruments, New Castle, DE, USA) in a single cantilever configuration. Rectangular specimens of cross-section 5 x 2 mm$^2$ and a gauge length of 17.5 mm were subjected to dynamic strain of 0.1% at a frequency of 1 Hz. The test was conducted within a temperature range of – 50 °C to 100 °C for the neat HDPE and – 50 °C to 80 °C for the PE-50SA/EG14 composite. A heating and cooling rate of ± 3 °C/min was applied, imposing an isotherm of 5 min before cooling. During the isotherm of the PE-50SA/EG14 specimen, the clamp was re-tightened at 80 °C to restore the grip.

Three-point bending tests were performed according to the ASTM D790-17 standard [28] using an Instron 5969 (Instron, Pianezza, Italy) equipped with a load cell of 1 kN and a thermostatic chamber. To evaluate the material performance across different thermal regimes, tests were performed at 0 °C, 25 °C, and 50 °C in a controlled environment with 50% of relative humidity. The test was conducted on bars of dimensions 5 x 2 x 45 mm$^3$, using a span length of 32 mm and a testing speed of 0.853 mm/min. Before testing, specimens were conditioned for 2 h within the thermal chamber to ensure thermal equilibrium. From the resulting stress–strain curves, the flexural elastic modulus ($E_f$) was calculated in the range 0.1 – 0.4% strain, and the flexural strength at 5% of strain ($S_{5\%}$) was determined. Results are reported as the mean value ± standard deviation of the 5 tested specimens.

Finally, the Vicat Softening Temperature (VST) was determined following the ASTM D1525-17e1 standard [29], using an HDT-Vicat tester model MP/3 (ATS FAAR Industries srl, Milano, Italy). A load of 10 N was applied at a heating rate of 2 °C/min. The VST values are reported as mean value ± standard deviation of three tested specimens.





## 3. Results and discussion

This section provides a comprehensive analysis of the 3D-printed product, followed by a critical discussion of the results in the context of existing literature. The characterization follows a multiscale approach: beginning from an examination of morphology and microstructure, progressing to the thermal and thermophysical properties, and concluding with an evaluation of the mechanical and thermo-mechanical behaviour of the composite material.

### 3.1. Morphology and product features

The morphological features of the final composite are illustrated in Fig. 4. Specifically, Fig. 4a displays a specimen designed for the LFA and leakage test, while Fig. 4b-d show a printed bar realized for determining the mechanical and thermo-mechanical properties.

Fig. 4 is representative of the appearance of the final samples, where the dominant graphite coloration indicates a high surface exposure of the conductive carbon planes. While the individual deposited layers are clearly discernible and can contribute to an increase in surface roughness, the deposition width and layer height remain consistent with the set parameters of 0.4 mm and 0.2 mm, respectively. Overall, the final products exhibit good consistency and geometrical stability, though surface regularity could be improved. As highlighted in Fig. 4d, small pores are visible at the layer junctions. These gaps are likely caused by slight variations in the filament diameter, which lead to an inconsistent flow of material during 3D-printing. These voids are a critical concern because they can weaken the material by acting as stress intensifiers and reduce heat transfer. To fix this, future work will focus on fine-tuning printing settings, such as the material flow rate and the overlap between layers.

The void fraction was quantified based on the apparent densities of PCM, HDPE, and printed material. These values, measured via helium pycnometry, are summarized in Table 3.

As expected, similar densities with high repeatability were determined for SA, HDPE, and PE-50SA/EG14. Considering the densities of SA and HDPE of Table 3 as the theoretical skeleton densities, the theoretical density ($\rho_{th}$) of 1.0562 g/cm$^3$ was determined for the composite material. When accounting for the effective composition derived from TGA, this value was refined to 1.0572 g/cm$^3$. The resulting void fraction, calculated with Equation (1), was 4.9 vol%. This value is consistent with the optical microscopy observations and represents a higher porosity compared to PE-70SA/EG14 composite produced by hot pressing [25]. This discrepancy is likely attributable to the inherent nature of the FFF process compared to the higher compaction pressures of hot pressing.

The morphological features of the single phases and their spatial distribution can be observed by SEM micrography of a fracture surface of the composite sample, as shown in Fig. 5 and in the Appendix (Fig. B.1).

The peculiar lamellar morphology of EG is clearly visible in well-distributed regions across the fracture surface (Fig. 5a). However, the lack of evident percolation among the graphitic layers suggests that the EG loading could be further increased. Distinguish between HDPE and SA phases proved more challenging, as no concentration of a single phase or PCM flakes emerged. HDPE, which in Fig. 5b is recognizable in the form of interconnected fibrils (brighter regions), appears uniformly

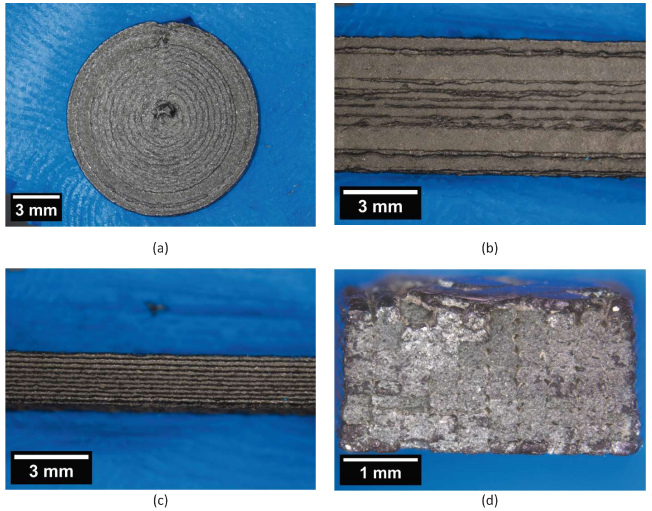


**Fig. 4.** Optical micrographs of the additively manufactured products: a) disk of diameter 12.7 mm; b) top-view of a bar of dimensions 45 x 5 x 2 mm$^3$; c) side-view of a bar of dimensions 45 x 5 x 2 mm$^3$ illustrating the deposited layer architecture; d) cross-sectional view of the fracture surface of a bar (5 x 2 mm$^2$).

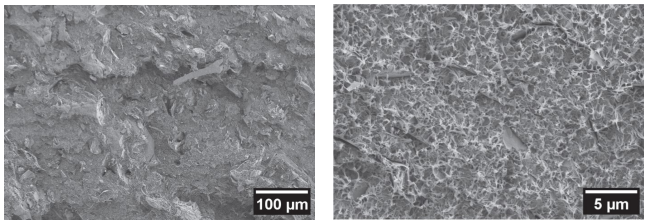


**Fig. 5.** SEM micrographs of a fracture surface of printed PE-50SA/EG14: a) low-magnification view showing the homogeneous distribution of the constituent phases; b) high-magnification view highlighting the interconnected HDPE ligament structure providing mechanical cohesion to the EG/PCM network.

distributed, confirming its role as the continuous matrix for the composite material. These observations are consistent with the behaviour of the bulk material counterpart, which maintained structural integrity even at a lower HDPE content of 30 wt% [25].

Complementing the morphological characterization, thermogravimetric analysis (TGA) was employed to evaluate the thermal stability and effective composition of the 3D-printed composite. The constituent weight fractions of the PE-50SA/EG14 sample were determined by analysing the intensity and position of the characteristic degradation peaks. Fig. 6 shows the TGA thermograms (a) and their derivatives (b), including a comparison with the PE-70SA/EG14 formulation previously fabricated via hot compression moulding [25]. The key thermal degradation results are summarized in Table 4.

The thermograms in Fig. 6 reveal the complete SA degradation in the range 150 – 320 °C, with a characteristic DTGA peak at 287 °C (Fig. 6b). The PCM degradation is partially postponed in the PE-50SA/EG14 composite. This phenomenon is a peculiar effect of the shape stabilization within closed structures [25,30,31]; conversely, this effect is absent in composites incorporating micro-encapsulated PCMs, as the confinement environment remains unchanged [13,30]. The thermal degradation of the HDPE matrix initiates after the complete degradation of SA, beginning at 400 °C, reaching a maximum rate at 502 °C, and goes to completion at 540 °C. Finally, as EG remains stable in the entire considered temperature interval [23], the residual mass at 700 °C can be attributed to the EG effective content.

The residual mass at 425 °C ($m_{425}$) was selected as a remarkable result because it corresponds to the inflection point in the mass loss of PE-50SA/EG14 (the minimum of the DTGA curve). At this temperature, the HDPE matrix remains essentially stable (99.3% of mass retention) and SA residues are negligible (0.9%); therefore, $m_{425}$ can be used to quantify the effective SA content in the composite by attributing the total mass loss to PCM degradation. A comparison between the nominal and effective compositions reveals a significant reduction in PCM content, from 43.9 wt% (Table 1) to 36.2 wt%. Consequently, the relative mass fraction of HDPE and EG, increased to 57.4 wt%, and 6.4 wt%, respectively. This discrepancy suggests that the initial PCM loading may have exceeded the retention capacity of the polymer-graphite matrix. Indeed, SA loss was observed during processing, specifically during the extrusion step, where a counterflow of molten PCM was noticed in the hopper. To achieve higher stable loadings in future optimizations, the formulation should be adjusted closer to the effective composition, or the EG-to-PCM ratio should be increased to enhance capillary stabilization. Based on the effective values, the printed composite is more accurately classified as PE-46SA/EG18, representing a concentration of 17.7 phr of EG relative to the SA.

To evaluate composition stability for thermal applications exceeding the melting temperature of PCM, a preliminary leakage test was performed at 60 °C, but no mass losses were registered over 48 h, remaining within the limits of the analytical balance threshold (±0.01%).

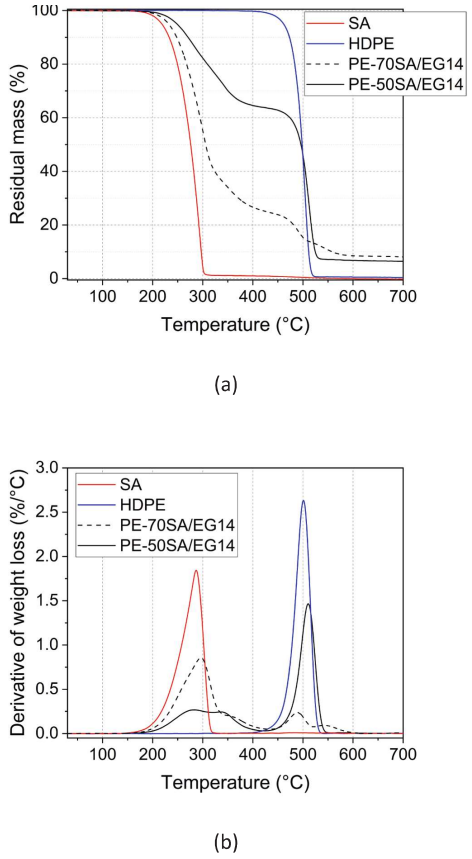


**Fig. 6.** TGA and DTGA thermograms: a) mass loss; b) derivative of weight loss (DTGA).

Conversely, an extended 150-hour-long leaking test at a higher





**Table 4**
Characteristic temperatures and mass loss data obtained from thermogravimetric analysis for neat components and composites.

| SAMPLE | $T_{5\%}$ (°C) | $T_{peak}$ (°C) | $m_{425}$ (%) | $m_{700}$ (%) |
|---|---|---|---|---|
| SA | 218.3 | 287.0 | 0.9 | 0 |
| HDPE | 461.5 | 501.6 | 99.3 | 0.4 |
| PE-70SA/EG14 [25] | 232.0 | 296.5 – 489.2 | 25.1 | 8.1 |
| PE-50SA/EG14 | 248.7 | 282.7 – 336.0 – 510.5 | 63.8 | 6.4 |

$T_{5\%}$ = temperature corresponding to the 5% of mass loss; $T_{peak}$ = thermal degradation peak temperature; $m_{425}$ = residual mass at 425 °C; $m_{700}$ = residual mass at 700 °C.

temperature of 70 °C evidenced a mass loss lower than 1.5 wt% for PE-50SA/EG14, as shown in Fig. 7.

After the first 24 h, the PCM loss reaches a plateau, indicating that the composite has stabilized. The material demonstrates excellent retention capacity, yielding a final mass loss of − 1.3 ± 0.2%. This analysis yields an actual composition of 34.9 wt% SA and 18.3 phr of EG relative to the SA phase. Similar trends have been reported PCM shape-stabilizations in polymeric matrices, where initial negligible leakage is attributed to peripheral PCM excess [25,32]. Based on combined TGA and leakage characterization, the current 3D-printed composite can be classified as PE-45SA/EG18. For future performance scaling, a PE-60SA/EG18 formulation is hypothesized as an optimal candidate. The rationale for maintaining at least 18:100 as EG-to-PCM ratio is to provide sufficient capillary surface area to compensate for the higher PCM loading (60 wt%), thereby preventing exudation during the phase transition. This proposed composition aims to improve volumetric energy density while maintaining a stable conductive network capable of supporting the structural integrity of the component during service. Notably, the material maintained its geometrical stability during the leaking test. This confirms the possible direct application of PCM-integrated additively manufactured structures, offering a superior alternative to traditional 3D-printed macro-encapsulation for applications requiring complex geometries [33–35].

### 3.2. Thermophysical properties

The thermal performances of the PCM and its corresponding composite were evaluated by characterizing latent heat storage (melting and crystallization), sensible heat storage, and heat transfer properties, specifically specific heat capacity, thermal diffusivity, and thermal conductivity.

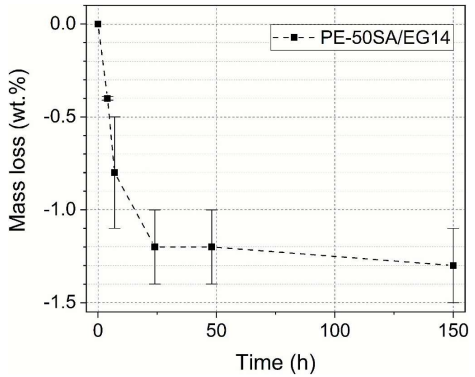


**Fig. 7.** Leakage test results conducted at 70 °C.

Phase transition temperatures and enthalpies were determined via Differential Scanning Calorimetry (DSC). Fig. 8 shows the thermograms for the neat PCM and the composite materials across the first heating (a), cooling (b), and second heating (c) scans, conducted at 1 °C/min. These results compare the 3D-printed sample with the only SA impregnated in

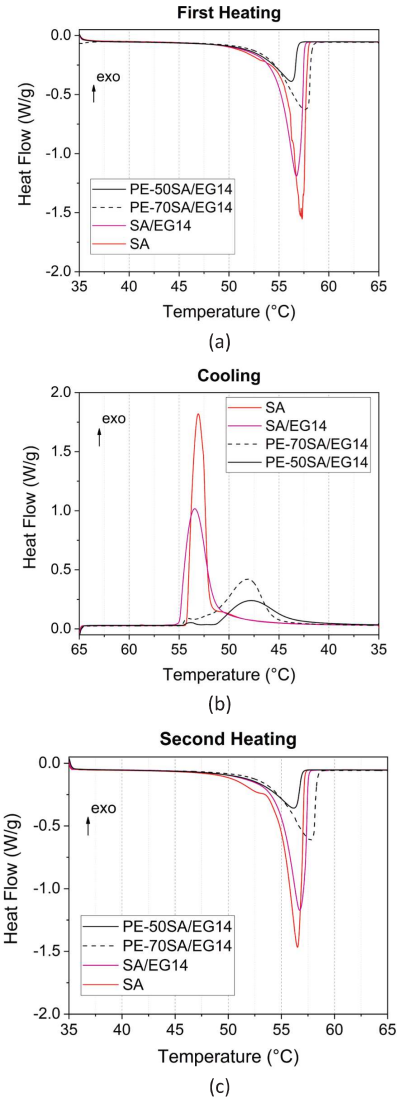


**Fig. 8.** DSC thermograms of neat SA, the SA/EG14 binary mixture, and the composites (PE-70SA/EG14 and PE-50SA/EG14) recorded at a scan rate of 1 °C/min: a) first heating; b) cooling; c) second heating.

EG (SA/14EG) and the preceding PE-70SA/EG14 sample produced by hot compression moulding [25]. Table 5 reports the characteristic parameters derived from the thermograms.

The melting enthalpy of the composite (70 J/g) is competitive within the current landscape of additively manufactured PCM composites, exceeding values reported in several recent studies [3,14,15,19], though it remains lower than the 132 J/g achieved using microencapsulated PCM in a commercial TPU matrix [36]. At this purpose it is wonder to observe that Zhu *et al.* recently synthetized a TPU with PEG as chain extender and chemical bonded PCM unit, reaching value of 94–131 J/g in the range 40–51 °C. Those authors produced flexible film for photothermal conversion, but their approach could be also an interesting opportunity for additive manufacturing [37].

Considering data of Table 5, the presence of EG and polyethylene decreased progressively the enthalpy in all the three steps of the cycle (1st heating – cooling – 2nd heating). The value of PE-50SA/EG14 corresponds to 38% of the latent heat of the neat PCM. Notably, the efficiency of melting is increased from 86% to approximatively 100% when the effective content of PCM is considered rather than the nominal loading. This alignment confirms the consistency between thermogravimetric and calorimetry dataset. To further enhance the total energy storage capacity without altering the weight fractions, SA could be replaced by alternative organic PCMs with higher latent heats, like paraffins or other commercial products. Regarding phase transition kinetics, while the melting range of PE-50SA/EG remains consistent with that of neat SA, the degree of supercooling is modified; specifically, crystallization is slightly hindered, resulting in a reduction of the crystallization temperature by nearly 5 °C.

To evaluate the cyclic reliability and long-term performance of the 3D-printed composite, 150 heating and cooling cycles were performed; a representative selection of these thermograms is shown in Fig. 9, while Table 6 lists the corresponding phase transition temperatures and enthalpies in heating and cooling.

The cyclic stability of the PE-50SA/EG14 composite provides critical insights into the interaction between the PCM and the HDPE/EG supporting network. As summarized in Table 6, the total melting enthalpy and the corresponding melting peak temperature remained remarkably constant throughout the 150 cycles. This stability indicates that the energy storage capacity is fully preserved (≥99%) and that no chemical degradation of the PCM occurred during repetitive thermal loading. These stable values demonstrate superior thermal reliability compared to the findings of Kumar et al., who reported a 4–7% reduction in enthalpy for nano-silica-based paraffin PCMs after 100 thermal cycles up to 80 °C [38,39].

Regarding the solidification process, the total released energy remained constant, but an evolution in the crystallization profile was observed. The enthalpy associated with the main crystallization peak at approximately 48 °C (highly confined PCM) slightly decreased over the cycles, while the secondary crystallization peak at approximately 55 °C (less confined PCM) showed a progressive increase in enthalpy reaching a plateau value after approximately 60 cycles. This phenomenon

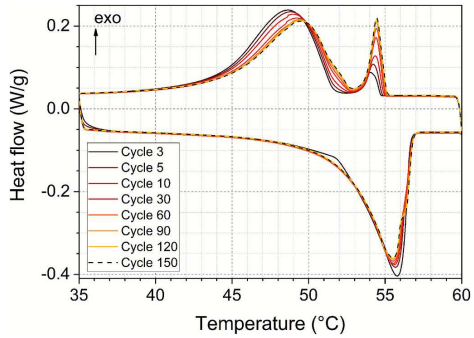


**Fig. 9.** Evolution of DSC thermograms for the 3D-printed PE-50SA/EG14 composite during repetitive thermal cycling (cycles 3 to 150) at a scan rate of 1 °C/min.

**Table 6**
DSC thermal properties obtained for the 3D-printed PE-50SA/EG14 composite across 150 heating/cooling cycles (at 1 °C/min), demonstrating the retention of phase transition temperatures and latent heat capacity over extended thermal cycling.

| Cycle number | $T_m$ (°C) | $\Delta H_m$ (J/g) | $T_c$ (°C) | $\Delta H_{c,TOT}$ (J/g) | $\Delta H_{c,FREE}$ (J/g) |
|---|---|---|---|---|---|
| 3 | 55.7 | 69.7 | 54.1 / 48.7 | 69.5 | 3.4 |
| 5 | 55.6 | 69.7 | 54.3 / 48.9 | 69.5 | 4.1 |
| 10 | 55.5 | 69.7 | 54.4 / 49.1 | 69.5 | 5.6 |
| 30 | 55.5 | 69.6 | 55.0 / 49.3 | 69.4 | 7.4 |
| 60 | 55.4 | 69.7 | 55.0 / 49.4 | 69.5 | 8.7 |
| 90 | 55.4 | 69.7 | 54.5 / 49.5 | 69.6 | 9.5 |
| 120 | 55.4 | 69.7 | 54.5 / 49.5 | 69.5 | 9.9 |
| 150 | 55.4 | 69.6 | 54.5 / 49.4 | 69.5 | 10.1 |

$T_m$ = melting peak temperature; $\Delta H_m$ = specific melting enthalpy; $T_c$ = crystallization peaks temperature; $\Delta H_{c,TOT}$ = total specific melting enthalpy during cooling; $\Delta H_{c,FREE}$ = specific melting enthalpy of free PCM during cooling.

suggests a gradual reorganization of the PCM within the HDPE/EG porous structure, where a fraction of the PCM transitions from a highly confined state to one that more closely mirrors the crystallization kinetics of the neat PCM and SA/EG14 composite (comparing with Fig. 8b). Importantly, the total crystallization enthalpy (calculated as the sum of both peaks) remained constant, as well as the melting one. This conservation of energy (≥99%), combined with the 1.3% mass loss plateau observed in leakage tests (Fig. 7), suggests that this PCM composite maintains a very good long-term thermal reliability without losing storage capacity.

Transitioning from latent heat storage to sensible heat storage and

**Table 5**
Summary of the DSC thermal properties obtained at a scan rate of 1 °C/min.

| SAMPLE | $T_{m1}$ (°C) | $\Delta H_{m1}$ (J/g) | $T_c$ (°C) | $\Delta H_c$ (J/g) | $T_{m2}$ (°C) | $\Delta H_{m2}$ (J/g) | $PCM_{m2}^{eff}$(%) | $\eta_{m2}$(%) |
|---|---|---|---|---|---|---|---|---|
| SA | 56.8 | 182.3 | 53.7 | 182.8 | 56.0 | 183.6 | 100 | 100 |
| SA/EG14 | 56.4 | 157.1 | 53.7 | 156.5 | 56.4 | 157.2 | 85.6 | 97.6 |
| PE-70SA/EG14 | 57.5 | 114.4 | 48.3 | 112.1 | 57.6 | 112.2 | 61.1 | 99.5 |
| PE-50SA/EG14 | 56.1 | 69.7 | 47.9 | 69.2 | 56.1 | 69.6 | 37.9 | 86.4 |

$T_{m1}$ = melting peak temperature during the first heating scan; $\Delta H_{m1}$ = specific melting enthalpy during the first heating scan; $T_c$ = crystallization main peak temperature during cooling; $\Delta H_c$ = specific melting enthalpy during cooling; $T_{m2}$ = melting peak temperature during the second heating scan; $\Delta H_{m2}$ = specific melting enthalpy during the second heating scan; $PCM_{m2}^{eff}$ = effective PCM content from the second melting transition (Equation (1)); $\eta_{m2}$ = efficiency of melting in the second heating scan (Equation (2)).





transport properties, the evaluation of thermal conductivity requires a precise identification of the material density profile as a function of temperature. The evaluated Coefficients of Volumetric Thermal Expansion (CVTE) are summarized in Table 7, while the resulting temperature-dependent bulk density profiles are shown in Fig. 10a.

Between 50 and 60 °C, the density values of SA were not evaluated because of the phase transition. Notably, no abrupt jump in density was observed, a finding that contrasts with producer datasheets and the majority of the works studying PCMs, which typically declare volume changes of 10–20% upon the phase transition [40,41]. This discrepancy can probably be attributed to the usual density determination near room temperature and well above the PCM melting point; such an approach often calculates density differences across a wide temperature gradient, thereby overlooking the continuous temperature trend as the material approaches the phase transition. Furthermore, the bulk density evaluated for the solid SA at 20 °C is significantly lower than the apparent density determined with the pycnometry, evidencing an interconnecting open porosity of 13 vol%, which is consistent with the formation of shrinkage cavities upon solidification.

The specific heat capacities, determined for comparison of a sapphire reference in DSC at 1 °C/min, are shown in Fig. 10b. Within the phase transition interval (40 – 65 °C), the specific heat capacity values are not reported as they are mathematically indetermined, theoretically tending towards infinity due to the latent heat contribution. The typical steep increase in specific heat capacity is observable as an incipient melting effect occurring several degrees below the appreciable transition [24]. The $c_p$ values for the neat PCM and HDPE are consistent with previously reported data [23,25], while the 3D-printed composite exhibits slightly higher values. Notably, the specific heat capacity increase is less pronounced in the liquid state than in the solid state; however, for the 3D-printed material, the trend diverges as it approaches the incipient melting of the HDPE matrix.

The thermal diffusivity trend as a function of temperature is presented in Fig. 10c. In agreement with previous studies [24], thermal diffusivity follows an inverse trend with respect to the specific heat capacity, showing an apparent decrease during the phase transition. Although the LFA software may generate numerical values in this region, the phase transition should be considered an undetermined regime for thermal diffusivity as well as for specific heat capacity. A clear increase in the thermal diffusivity is observed for the printed composite compared to the neat PCM, confirming the beneficial role of the EG in enhancing the thermal transport properties.

Thermal conductivity was determined at each temperature as the product of the previous thermophysical properties, according to Equation (5) (Fig. 10d). The neat PCM maintains a relatively constant thermal conductivity across the temperature range, a counterintuitive trend consistent with prior findings [24] where the temperature dependence of thermal diffusivity and specific heat capacity effectively neutralize one other. The incorporation of EG significantly enhances the thermal conductivity, especially in the solid state, where the PE-50SA/EG14 composite shows an improvement of 320% to 350% over the neat SA. While this enhancement is lower than that achieved via hot pressing (900%), probably because of the higher HDPE content (50 wt%) required for printability compared to the previous work (30 wt%) [25],

**Table 7**
Coefficients of Volumetric Thermal Expansions (CVTE) for the 3D-printed composite and neat components as a function of temperature, highlighting the expansion behaviour across the solid and liquid states.

| CVTE [°C$^{-1}$] | Temperature range [°C] | | |
|---|---|---|---|
| | 10 – 30 | 30 – 60 | 60 – 90 |
| HDPE | $3.7 \cdot 10^{-4}$ | $3.7 \cdot 10^{-4}$ | $3.7 \cdot 10^{-4}$ |
| SA | $8.2 \cdot 10^{-4}$ | $8.2 \cdot 10^{-4}$ | $6.9 \cdot 10^{-4}$ |
| PE-50SA/EG14 | $2.6 \cdot 10^{-4}$ | $9.6 \cdot 10^{-4}$ | $7.7 \cdot 10^{-4}$ |

this study represents the first successful enhancement in thermal conductivity in a PCM-based composite produced via additive manufacturing of a thermoplastic polymer. At the PCM liquid state, the thermal conductivity enhancement remains significant, on the order of 200%. The punctual values of thermophysical properties from Fig. 10 are summarized in Table C.1.

To evaluate the suitability of the developed composites for space-constrained thermal management, a holistic performance comparison is presented in Table 8. A specific Figure of Merit (FoM) was employed to quantitatively assess the synergy between the thermal conductivity enhancement and the retention of volumetric energy density. This approach addresses the inherent trade-off in PCM composites, where the addition of a conductive filler (EG) typically displaces the latent heat-storing phase.

As evidenced by the data, SA/EG14 represents the optimal configuration; at this ratio, the FoM is maximized as the thermal conductivity reaches a plateau, while the volumetric energy storage capacity remains high enough to ensure effective thermal buffering. Beyond this concentration, the marginal gains in heat transfer do not justify the significant reduction in energy density, confirming the SA-to-EG ratio selection as the most balanced solution for high-performance applications. Furthermore, this specific ratio ensures superior long-term PCM retention compared to composites with lower EG content [23]. The benefits of the synergy between EG and HDPE—rather than using HDPE alone—are further evidenced in Table 8. Specifically, the PE-50SA composite characterized in a previous study [25] exhibits a FoM of $0.44 \cdot 10^4$ lower than that of neat SA ($0.56 \cdot 10^4$), highlighting the essential role of EG in overcoming the thermal limitations of the simple-polymer matrix. From a manufacturing perspective, the formulation demonstrates excellent processability at 50 wt% HDPE, enabling the fabrication of complex geometries without significantly compromising the FoM. Future work will aim to reduce the HDPE fraction and evaluate the feasibility of processing PE-60SA/EG18 via Fused Filament Fabrication (FFF), being FoM up to $1.3 \cdot 10^4$. This will involve optimizing printing parameters and exploring the use of extrusion-grade polyethylene to enhance performance.

### 3.3. Dynamomechanical and mechanical properties

To evaluate the mechanical performances of the 3D-printed material across a broad temperature range, DMA tensile test, quasi-static three-point bending test, and Vicat softening temperature measurements were performed, with results compared against compression-molded HDPE.

Initially, the mechanical stiffness was characterized via DMA to evaluate the influence of the PCM on thermomechanical properties, not only before and after melting, but also during crystallization. A non-conventional heating and cooling cycle was adopted for this purpose. It was observed that upon the complete melting of the PCM, the composite material undergoes localized relaxation and partial collapse, leading to a reduction in the clamping force, which, for this reason, was quickly fixed before the cooling ramp. The storage modulus (E'), the loss modulus (E"), and the damping factor (tan δ) are presented in Fig. 11.

For both the neat HDPE and the 3D-printed composite, the storage modulus decreased during heating and recovered during cooling (Fig. 11a), accompanied by corresponding E" peaks (Fig. 11b), and increasing or decreasing damping during heating or cooling, respectively (Fig. 11c). Typically, polyethylene exhibits three main transitions: the γ-transition, that is attributed to the glass transition temperature and occurs between −130/−110 °C [42]; the β-transition in the range −50/0 °C, that is related to the polymer branching and it is almost no detectable in HDPE [43]; the α-transition, that is evidenced in the range 20/70 °C and it is associated to the molecular motions within crystals and interfacial regions of lamellae. This reversible α-transition [44,45] is well documented in the sigmoidal flexural storage modulus curves of HDPE, showing a maximum shift of about −25 °C from heating to cooling, and in the E" peaks at about 49 °C and 25 °C in heating and

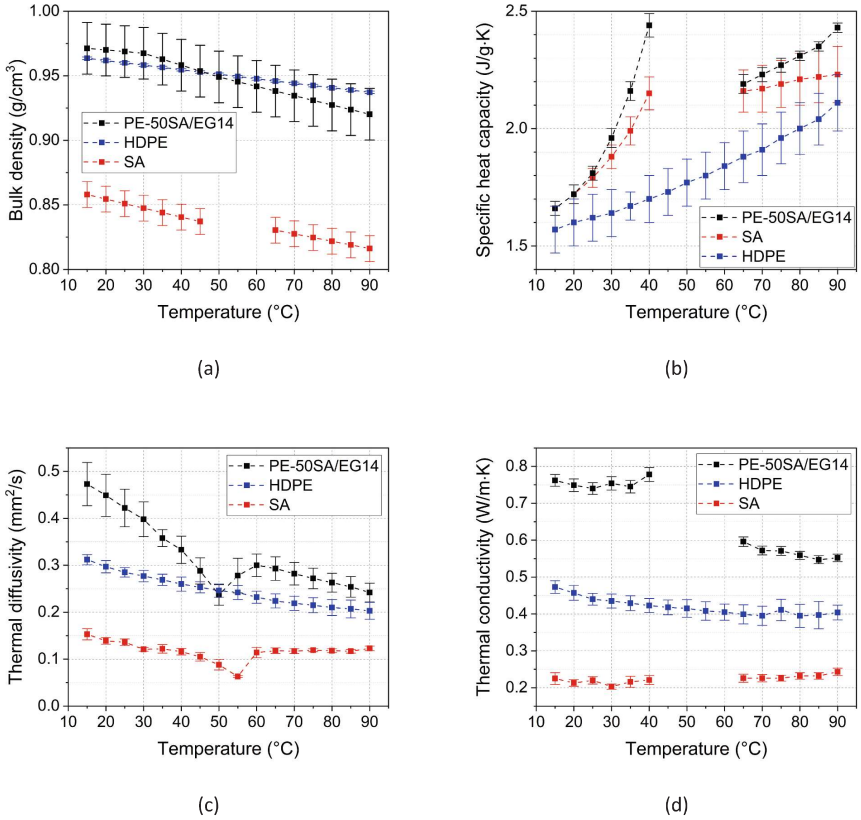


**Fig. 10.** Temperature-dependent thermophysical properties (15–90 °C) for neat SA, neat HDPE, and 3D-printed composites: a) bulk density; b) specific heat capacity; c) thermal diffusivity; d) thermal conductivity.

**Table 8**
Comparison of the Figure of Merit (FoM) at 30 °C for various compositions, highlighting the balance between latent heat storage capacity and thermal conductivity in the 3D-printable formulation, according to Equation (5).

| Sample | $\Delta H_m^*$ (J/cm³) | λ (W/m·K) | FoM (W/(m².K$^{0.5}$.s$^{0.5}$)) |
|---|---|---|---|
| SA | 156 | 0.20 ± 0.01 | 0.56 · 10⁴ |
| SA/EG10 | 152 | 5.1 ± 0.5 | 2.86 · 10⁴ |
| SA/EG12 | 151 | 6.5 ± 0.6 | 3.15 · 10⁴ |
| SA/EG14 | 150 | 7.3 ± 0.4 | 3.31 · 10⁴ |
| SA/EG16 | 149 | 7.2 ± 0.7 | 3.27 · 10⁴ |
| SA/EG18 | 148 | 7.1 ± 0.8 | 3.22 · 10⁴ |
| SA/EG20 | 147 | 7.1 ± 0.6 | 3.23 · 10⁴ |
| SA/EG25 | 144 | 7.2 ± 0.7 | 3.17 · 10⁴ |
| PE-50SA [25] | 49 | 0.39 ± 0.02 | 0.44 · 10⁴ |
| PE-70SA/EG14 [25] | 119 | 1.65 ± 0.12 | 1.40 · 10⁴ |
| PE-50SA/EG14 | 68 | 0.75 ± 0.02 | 0.71 · 10⁴ |
| PE-60SA/EG18[i] | 99 | 1.1 – 1.6 | 1.0 · 10⁴ –1.3 · 10⁴ |

[i] Proposed optimized composition for future development, highlighting formulations considering a thermal conductivity consistently intermediate between PE-50SA/EG14 and PE-70SA/EG18.

cooling, respectively.

The PE-50SA/EG14 composite exhibited similar E' profiles, though shifted toward lower temperatures. Specifically, the correspondent E'' peaks for the composite decreased to 39 °C (heating) and 15 °C (cooling), approximately 10 °C lower than those of neat HDPE. These peaks can be attributed to the almost simultaneous occurrence of the HDPE α-transition and the first-order transitions of PCM. A thermal delay can be noted between the heating and cooling cycles by comparing the endset and the onset of E' and E'', respectively, with a temperature difference of about 10 °C for HDPE and 20 °C for the composite, underscoring the influence of the PCM melting and crystallization kinetics when confined within the HDPE (consistent with DSC curves performed at 1 °C/min in Fig. 8). The damping factor curves (Fig. 11c) show more pronounced differences: the PCM composite exhibit a higher slope, a wider hysteresis-like loop, and significantly higher absolute values (0.20–0.30) compared to HDPE (about 0.15–0.18 above the end of α-transition). These findings stem from the increased molecular mobility during the PCM phase transition, as tan δ is highly sensitive to all dissipation factors. The apparent anomalous tan δ peaks in PE-50SA/EG14 at 60–70 °C (heating) and 45–25 °C (cooling) are directly





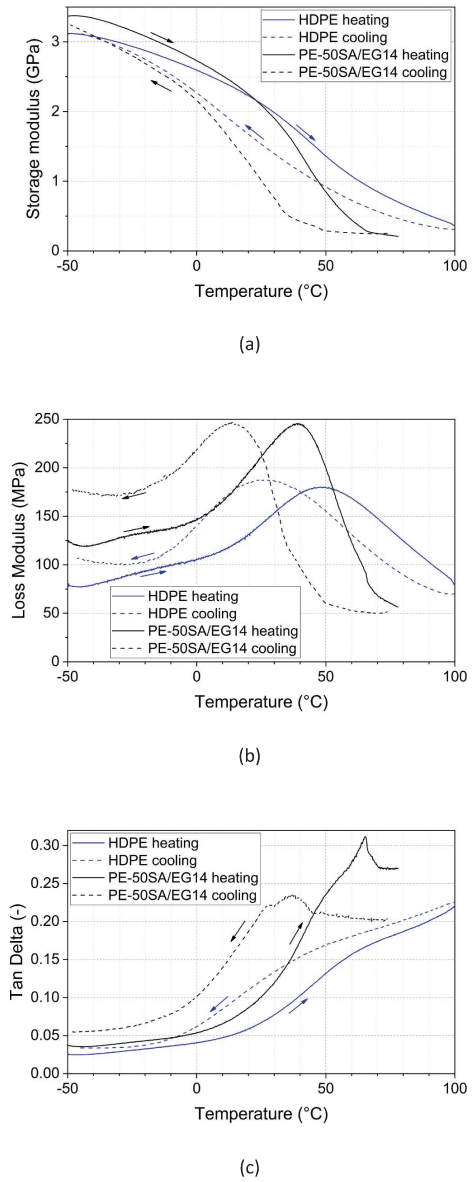


**Fig. 11.** Dynamic Mechanical Analyses (DMA) thermograms of neat HDPE and 3D-printed composite during heating and cooling at 3 °C/min: a) Storage modulus (E'); b) Loss modulus (E''); c) Damping factor (tan δ).

correlated with the melting and crystallization of the PCM, as further supported by the DSC thermograms in Fig. S2.

Following the DMA analysis, which clearly evidenced a temperature-dependent decrease in stiffness — more pronounced in the PE-50SA/EG14 composite than in the neat HDPE due to sharper and more intense transitions— quasi-static mechanical properties were further evaluated. Three-point bending tests were conducted at 23 °C (room temperature), 0 °C, and 50 °C to capture the material behaviour across these critical transition points. Fig. 12a illustrates a 3D-printed specimen at maximum flexural deflection prior to slippage at room temperature. The characteristic flexural stress–strain curve at 23 °C for the 3D-printed material and hot-pressed neat HDPE are compared in Fig. 12b, while the corresponding curves at 0 °C and 50 °C are provided in the Supplementary information (Fig. S3). As expected, a direct correlation was observed: increasing the temperature resulted in a reduced flexural modulus and an increase in material flexibility.

None of the specimens failed during the test at room temperature, demonstrating the high flexibility afforded by the HDPE matrix, as evidenced in Fig. 12a. In accordance with the ASTM E1269-11 standard [26], which specifies a 5% strain limit for non-breaking specimens, the flexural strength was evaluated at this standardized point. In contrast, the composite material exhibited brittle behaviour at 0 °C, reaching a flexural strength of 16.3 ± 1.2 MPa with strain at break of only 1.4 ± 0.2% (see Fig. S3a). The primary flexural results, including the comparative elastic modulus and strength across the three selected temperatures, are summarized in Table 9.

The results of Table 9 evidence a slight reduction in elastic modulus compared to neat HDPE, while the flexural strength is significantly reduced. However, the strength remains comparable to that of the bulk (hot-pressed) version containing 30 wt% of HDPE, while maintaining a ductile failure mode owing to the HDPE matrix. Higher PCM loadings would likely lead to material embrittlement.

Finally, the maximum service temperature was evaluated through the Vicat Softening Temperature (VST), which identifies the point at which the material can no longer withstand tip penetration without structural collapse. The VST of the printed composite was 91 ± 5 °C (see Fig. S4). While this is lower than that of neat HDPE (128 ± 5 °C), it exceeds the values reported for all previously studied formulations [25], further demonstrating the synergistic role of HDPE and EG as a supporting matrix for the PCM.

The comprehensive mechanical characterization—encompassing DMA, flexural testing, and VST— reveals temperature-dependent properties that, when combined with thermophysical data, provide a robust framework for application-specific design. The structural design of the components is engineered to withstand relevant mechanical stresses during assembly. Under service conditions, the operational profile exposes the part to limited loads, thereby preserving structural integrity and ensuring a significant safety margin throughout its lifecycle.

## 4. Conclusions

This study presents, for the first time, a streamlined process for integrating non-microencapsulated PCM into additive manufacturing through a dual shape stabilization strategy utilizing expanded graphite (EG) and HDPE. The composition and processes enabling the fabrication of highly conductive components via Fused Filament Fabrication (FFF) have been described in detail. The primary contributions of this work, are summarized as follow:

- the use of HDPE as a printable matrix effectively prevents PCM thermal degradation during processing;
- the composite exhibits contained PCM leakage, which extinguishes after the initial hours of thermal cycling;
- the 3D-printed material reveals a thermal management capacity at the transition temperature (50–60 °C) of 70 J/g;

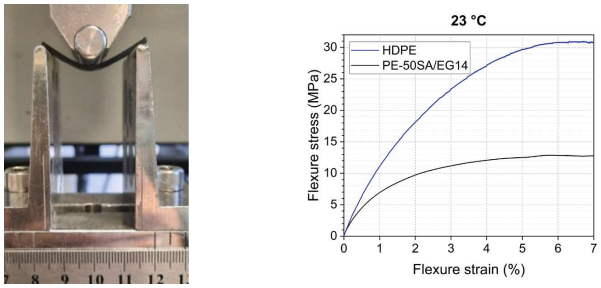


**Fig. 12.** Flexural properties determined via three-point bending tests: a) visual evidence of the high ductility and deformation capacity of the PE-50SA/EG14 specimen near 5% strain at 23 °C; b) representative stress–strain curves comparing the 3D-printed composite with neat HDPE at 23 °C.

**Table 9**
Mechanical properties of the 3D-printed composite derived from three-point bending tests at 0 °C, 23 °C (room temperature), and 50 °C.

| Sample | $E_F$(GPa) | | | $S_{5\%}$(MPa) | | |
|---|---|---|---|---|---|---|
| | 0 °C | 23 °C | 50 °C | 0 °C | 23 °C | 50 °C |
| HDPE | 1.89 ± 0.20 | 1.22 ± 0.08 | 0.63 ± 0.04 | 47.4 ± 3.4 | 28.6 ± 1.5 | 15.3 ± 1.5 |
| PE-50SA/EG14 | 1.49 ± 0.16 | 0.83 ± 0.02 | 0.24 ± 0.05 | / | 13.3 ± 1.3 | 4.8 ± 0.5 |
| Ratio | 0.79 | 0.72 | 0.38 | 0.72* | 0.46 | 0.31 |

$E_F$ = flexural elastic modulus; $S_{5\%}$ = flexural strength at 5% of strain
*16/22 at 1.6% of strain

- for the first time, an additively manufactured PCM composite demonstrates significantly enhanced thermal conductivity, reaching 0.8 W/m·K;
- the trade-off between thermal conductivity enhancement and the reduction in energy density (resulting from the integration of PCM into a printable matrix) is successfully balanced and quantified through an enhanced Figure of Merit;
- the synergistic combination of HDPE and EG ensures high structural integrity, allowing the components to withstand assembly loads while maintaining a high safety margin under restricted operational stresses.

In summary, this work identifies an optimized formulation for FFF production of a stabilized composite containing 36 wt% of palmitic/stearic acid mixture. The synergistic effect of EG and HDPE in confining organic PCM enables the realization of complex geometries that can streamline the production of thermal management systems with a high exchange surface area via additive manufacturing.

Looking forward, these results suggest that increasing the PCM fraction to 60 wt% will require a proportional increase in EG content (to 18 phr in PCM) to ensure effective stabilization. Future research will focus on the selection of higher-viscosity PE grades to accommodate this increased PCM loading while maintaining at least 18:100 of EG-to-PCM ratio—exemplified by the PE-60PCM/EG18 formulation—to balance maximized energy storage with the mechanical and thermal stability required for long-term service.

## CRediT authorship contribution statement

**Sereno Sacchet:** Writing – original draft, Validation, Methodology, Investigation, Formal analysis, Data curation, Conceptualization. **Mirko Coser:** Writing – review & editing, Validation, Methodology, Investigation, Formal analysis, Conceptualization. **Francesco Valentini:** Writing – review & editing, Validation, Methodology, Conceptualization. **Maurizio Grigiante:** Methodology, Conceptualization. **Riccardo Po:** Writing – review & editing, Supervision, Methodology, Funding acquisition, Conceptualization. **Luca Fambri:** Writing – review & editing, Validation, Supervision, Methodology, Funding acquisition, Conceptualization.

## Declaration of competing interest

The authors declare that they have no known competing financial interests or personal relationships that could have appeared to influence the work reported in this paper.

## Appendix

*Supporting grid as the basement of the AM products*

Fig. A.1 shows the two-layer raft designed to facilitate the detachment of the specimen from the plate.





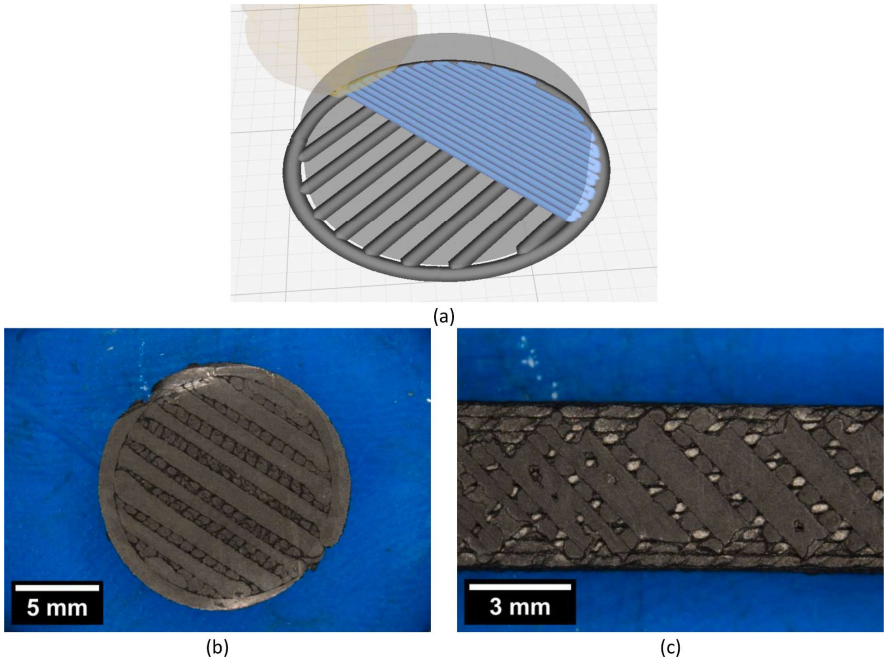


**Fig. A1.** Two-layer raft basement utilized for 3D-printed products: a) digital design model generated in Ultimaker Cura; b) photograph of the printed supporting raft for the disk-shaped specimen; c) photograph of the printed supporting raft for the bar-shaped specimen.

*Scanning electron microscopy (SEM) additional micrography*

To further evidence the EG dispersion in HDPE matrix, Fig. B.1 shows two PE-50SA/EG14 SEM micrographs at intermediate magnifications, as a complement to Fig. 5.

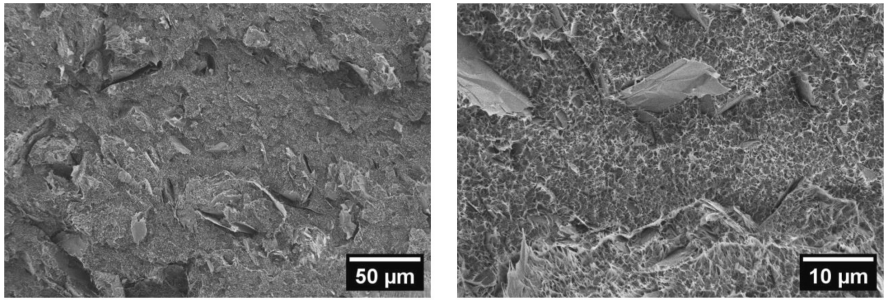


**Fig. B1.** Additional SEM micrographs of the 3D-printed PE-50SA/EG14 fracture surface at intermediate magnification, providing a broader field of view of the homogeneous dispersion of the EG/PCM clusters within the HDPE matrix.

*Thermophysical properties summary*

Table C.1 summarizes the thermophysical properties of the neat SA and the printed composite PE-50SA/EG14 as a function of temperature.

**Table C1**
Comparative summary of the thermophysical properties for the neat PCM (SA) and the 3D-printed PE-50SA/EG14 composite, highlighting the performance enhancements across both solid and liquid phases.

| Temperature (°C) | $\rho$ (g/cm$^3$) | | $c_p$ (J/g·K) | | $\alpha$ (mm$^2$/s) | | $\lambda$ (W/m·K) | |
|---|---|---|---|---|---|---|---|---|
| | SA | PE-50SA/EG14 | SA [46] | PE-50SA/EG14 | SA [46] | PE-50SA/EG14 | SA | PE-50SA/EG14 |
| 15 | 0.86 ± 0.01 | 0.97 ± 0.02 | 1.66 ± 0.03 | 1.66 ± 0.03 | 0.153 ± 0.012 | 0.472 ± 0.046 | 0.225 ± 0.016 | 0.762 ± 0.016 |
| 20 | 0.86 ± 0.01 | 0.97 ± 0.02 | 1.72 ± 0.04 | 1.72 ± 0.04 | 0.139 ± 0.007 | 0.449 ± 0.045 | 0.213 ± 0.009 | 0.749 ± 0.017 |
| 25 | 0.85 ± 0.01 | 0.97 ± 0.02 | 1.79 ± 0.04 | 1.81 ± 0.03 | 0.136 ± 0.007 | 0.422 ± 0.040 | 0.220 ± 0.010 | 0.740 ± 0.016 |
| 30 | 0.85 ± 0.01 | 0.97 ± 0.02 | 1.88 ± 0.05 | 1.96 ± 0.04 | 0.121 ± 0.004 | 0.398 ± 0.037 | 0.203 ± 0.007 | 0.754 ± 0.018 |
| 35 | 0.85 ± 0.01 | 0.96 ± 0.02 | 1.99 ± 0.06 | 2.16 ± 0.04 | 0.122 ± 0.009 | 0.358 ± 0.018 | 0.216 ± 0.015 | 0.745 ± 0.017 |
| 40 | 0.84 ± 0.01 | 0.96 ± 0.02 | 2.15 ± 0.07 | 2.44 ± 0.05 | 0.116 ± 0.007 | 0.333 ± 0.029 | 0.221 ± 0.012 | 0.778 ± 0.019 |
| 45 | 0.84 ± 0.01 | 0.95 ± 0.02 | – | – | 0.105 ± 0.009 | 0.288 ± 0.028 | – | – |
| 50 | – | 0.95 ± 0.02 | – | – | 0.088 ± 0.011 | 0.237 ± 0.022 | – | – |
| 55 | – | 0.95 ± 0.02 | – | – | 0.063 ± 0.002 | 0.278 ± 0.037 | – | – |
| 60 | – | 0.94 ± 0.02 | – | – | 0.114 ± 0.011 | 0.300 ± 0.024 | – | – |
| 65 | 0.83 ± 0.01 | 0.94 ± 0.02 | 2.16 ± 0.09 | 2.19 ± 0.04 | 0.118 ± 0.006 | 0.293 ± 0.025 | 0.226 ± 0.011 | 0.596 ± 0.013 |
| 70 | 0.83 ± 0.01 | 0.93 ± 0.02 | 2.17 ± 0.10 | 2.23 ± 0.03 | 0.117 ± 0.005 | 0.282 ± 0.024 | 0.226 ± 0.010 | 0.572 ± 0.012 |
| 75 | 0.83 ± 0.01 | 0.93 ± 0.02 | 2.19 ± 0.10 | 2.27 ± 0.03 | 0.119 ± 0.003 | 0.272 ± 0.022 | 0.226 ± 0.008 | 0.571 ± 0.012 |
| 80 | 0.82 ± 0.01 | 0.93 ± 0.02 | 2.21 ± 0.11 | 2.31 ± 0.02 | 0.118 ± 0.004 | 0.263 ± 0.020 | 0.232 ± 0.009 | 0.559 ± 0.011 |
| 85 | 0.82 ± 0.01 | 0.92 ± 0.02 | 2.22 ± 0.11 | 2.35 ± 0.02 | 0.117 ± 0.004 | 0.254 ± 0.022 | 0.232 ± 0.009 | 0.547 ± 0.011 |
| 90 | 0.82 ± 0.01 | 0.92 ± 0.02 | 2.23 ± 0.12 | 2.43 ± 0.02 | 0.123 ± 0.005 | 0.242 ± 0.020 | 0.243 ± 0.010 | 0.552 ± 0.010 |

## Appendix A. Supplementary data

Supplementary data to this article can be found online at https://doi.org/10.1016/j.tsep.2026.104596.

## Data availability

Data will be made available on request.

## References


[1] T.B. Freeman, K.E.O. Foster, C.J. Troxler, C.W. Irvin, A. Aday, S.K.S. Boetcher, A. Mahvi, M.K. Smith, A. Odukomaiya, Advanced materials and additive manufacturing for phase change thermal energy storage and management: a review, Adv. Energy Mater. 13 (24) (2023) 2204208, https://doi.org/10.1002/aenm.202204208.

[2] Y. Er, O. Güler, A. Ustaoğlu, G. Hekimoğlu, A. Sarı, S. Subaşı, O. Gencel, M. Maraşlı, Characterisation and energy storage performance of 3D printed-photocurable resin/microencapsulated phase change material composite, Therm. Sci. Eng. Prog. 48 (2024) 102381, https://doi.org/10.1016/j.tsep.2023.102381.

[3] Y. Mao, T. Miyazaki, K. Sakai, J. Gong, M. Zhu, H. Ito, A 3D printable thermal energy storage crystalline gel using mask-projection stereolithography, Polymers (2018).

[4] Y. Cho, J. Kim, Enhanced thermal and mechanical properties of 3D-printed PEG containing acrylate composite with surface-treated BN via digital light processing, Polym. Test. 118 (2023) 107898, https://doi.org/10.1016/j.polymertesting.2022.107898.

[5] C. Wang, C. Liu, C. Li, Additive manufacturing of shape-stabilized composite phase change materials via ultraviolet curing, Addit. Manuf. 61 (2023) 103341, https://doi.org/10.1016/j.addma.2022.103341.

[6] I. Melendez, K.B. Morgan, C.J. Troxler, R.M. Rodriguez, S.K.S. Boetcher, Vat photopolymerization for thermal energy storage applications using encapsulated phase change material suspended in photocurable resin, Therm. Sci. Eng. Prog. 56 (2024) 102986, https://doi.org/10.1016/j.tsep.2024.102986.

[7] Z. Zhou, Z. Hu, D. Wang, H. Wu, Visualized-experimental investigation on the melting performance of PCM in 3D printed metal foam, Therm. Sci. Eng. Prog. 31 (2022) 101298, https://doi.org/10.1016/j.tsep.2022.101298.

[8] P. Wei, C.E. Cipriani, E.B. Pentzer, Thermal energy regulation with 3D printed polymer-phase change material composites, Matter 4 (6) (2021) 1975–1989, https://doi.org/10.1016/j.matt.2021.03.019.

[9] C.E. Cipriani, Y. Shu, E.B. Pentzer, C.C. Benjamin, Viscoelastic and thixotropic characterization of paraffin/photopolymer composites for extrusion-based printing, Phys. Fluids 34 (9) (2022), https://doi.org/10.1063/5.0104157.

[10] C.-P. Feng, K.-Y. Sun, J.-C. Ji, L. Hou, G.-P. Cui, Z.-G. Zhao, H.-B. Lan, 3D Printable, form stable, flexible phase-change-based electronic packaging materials for thermal management, Addit. Manuf. 71 (2023) 103586, https://doi.org/10.1016/j.addma.2023.103586.

[11] A. Cano-Vicent, M.M. Tambuwala, S.S. Hassan, D. Barh, A.A.A. Aljabali, M. Birkett, A. Arjunan, Á. Serrano-Aroca, Fused deposition modelling: current status, methodology, applications and future prospects, Addit. Manuf. 47 (2021) 102378, https://doi.org/10.1016/j.addma.2021.102378.

[12] D. Rigotti, A. Dorigato, A. Pegoretti, 3D printable thermoplastic polyurethane blends with thermal energy storage/release capabilities, Mater. Today Commun. 15 (2018) 228–235, https://doi.org/10.1016/j.mtcomm.2018.03.009.

[13] D. Rigotti, A. Dorigato, A. Pegoretti, Multifunctional 3D-printed thermoplastic polyurethane (TPU)/multiwalled carbon nanotube (MWCNT) nanocomposites for thermal management applications, Appl. Sci. 14 (20) (2024), https://doi.org/10.3390/app14209614.

[14] P. Singh, A. Odukomaiya, M.K. Smith, A. Aday, S. Cui, A. Mahvi, Processing of phase change materials by fused deposition modeling: Toward efficient thermal energy storage designs, J. Storage Mater. 55 (2022) 105581, https://doi.org/10.1016/j.est.2022.105581.

[15] R. Salgado-Pizarro, J.A. Padilla, E. Xuriguera, C. Barreneche, A.I. Fernández, Novel shape-stabilized phase change material with cascade character: synthesis, performance and shaping evaluation, Energies 14 (9) (2021), https://doi.org/10.3390/en14092621.

[16] K.E.O. Foster, T.B. Freeman, I. Lizier-Zmudzinski, S. Dudt, K.B. Morgan, S.K. S. Boetcher, A. Odukomaiya, Additive manufacturing of thermal energy storage composites with microencapsulated phase change materials supported in a multipolymer matrix, Adv. Eng. Mater. 27 (20) (2025), https://doi.org/10.1002/adem.202501289.

[17] C.G. Schirmeister, T. Hees, E.H. Licht, R. Mülhaupt, 3D printing of high density polyethylene by fused filament fabrication, Addit. Manuf. 28 (2019) 152–159, https://doi.org/10.1016/j.addma.2019.05.003.

[18] T.B. Freeman, M.A. Messenger, C.J. Troxler, K. Nawaz, R.M. Rodriguez, S.K. S. Boetcher, Fused filament fabrication of novel phase-change material functional composites, Addit. Manuf. 39 (2021) 101839, https://doi.org/10.1016/j.addma.2021.101839.

[19] T.B. Freeman, D. Spitzer, P.N. Currier, V. Rollin, S.K.S. Boetcher, Phase-change materials/HDPE composite filament: a first step toward use with 3D printing for thermal management applications, J. Therm. Sci. Eng. Appl. 11 (5) (2019), https://doi.org/10.1115/1.4042592.

[20] M. Nofal, Y. Pan, S. Al-Hallaj, Selective laser sintering of phase change materials for thermal energy storage applications, Procedia Manuf. 10 (2017) 851–865, https://doi.org/10.1016/j.promfg.2017.07.071.

[21] M. Nofal, S. Al-Hallaj, Y. Pan, Thermal management of lithium-ion battery cells using 3D printed phase change composites, Appl. Therm. Eng. 171 (2020) 115126, https://doi.org/10.1016/j.applthermaleng.2020.115126.

[22] M. Cao, J. Huang, Z. Liu, The enhanced performance of phase-change materials via 3D printing with prickly aluminum honeycomb for thermal management of ternary lithium batteries, Adv. Mater. Sci. Eng. 2020 (1) (2020) 8167386, https://doi.org/10.1155/2020/8167386.

[23] S. Sacchet, F. Valentini, A. Benin, M. Guidolin, R. Po, L. Fambri, Expanded graphite (EG) stabilization of stearic and palmitic acid mixture for thermal management of photovoltaic cells, C 10 (2) (2024), https://doi.org/10.3390/c10020046.

[24] S. Sacchet, F. Valentini, M. Guidolin, R. Po, L. Fambri, Shape-stabilized phase change materials with expanded graphite for thermal management of photovoltaic cells: selection of materials and preparation of panels, Appl. Sci. 15 (8) (2025), https://doi.org/10.3390/app15084352.

[25] S. Sacchet, F. Valentini, C. Rizzo, R. Po, L. Fambri, High density polyethylene with phase change materials for thermal energy management, Energy Mater. 5 (4) (2025) 500042, https://doi.org/10.20517/energymater.2024.112.

[26] ASTM E1269-11, 2018. https://www.astm.org/e1269-11.html. (Accessed 08 Nov 2025).







[27] P.J. Shamberger, Cooling Capacity figure of Merit for phase Change Materials, J. Heat Transfer 138 (2) (2015), https://doi.org/10.1115/1.4031252.

[28] ASTM D790-17, 2017. https://www.astm.org/standards/d790. (Accessed 08 Nov 2025).

[29] ASTM D1525-17e1 2017. https://www.astm.org/d1525-17e01.html. (Accessed 08 Nov 2025).

[30] S.J. Jaiswal, S.N. Sonare, P.A. Mahanwar, Thermal energy storage material based on high density polyethylene filled with graphene oxide modified microencapsulated eutectic mixture of fatty acid, J. Polym. Environ. 32 (1) (2024) 150–163, https://doi.org/10.1007/s10924-023-02990-z.

[31] H.J. Mombeki Pea, Z.J. An, X.Z. Du, T.L. Shi, D. Zhang, Structure, characterization and thermal properties of the form-stable paraffin/high-density polyethylene/expanded graphite/epoxy resin composite PCMs for thermal energy storage, J. Therm. Sci., 32(6) (2023) 2104-2114 doi: 10.1007/s11630-023-1800-4.

[32] F. Valentini, L. Fambri, A. Dorigato, A. Pegoretti, Production and characterization of TES-EPDM foams with paraffin for thermal management applications, Front. Mater. 8 (2021) 660656, https://doi.org/10.3389/fmats.2021.660656.

[33] M. Moreira, T. Silva, J. Dias-de-Oliveira, C. Amaral, F. Neto, Material extrusion 3D printing of leakproof capsules: experimental study on phase change material macroencapsulation, Next Mater. 7 (2025) 100461, https://doi.org/10.1016/j.nxmate.2024.100461.

[34] S. Nishad, H.M. Elmoughni, R.A. Shakoor, Z.A. Qureshi, B. Moossa, I. Krupa, A novel design for battery cooling based on highly thermally conductive phase change composites encapsulated by 3D printed polyethylene/boron nitride layer, J. Storage Mater. 112 (2025) 115490, https://doi.org/10.1016/j.est.2025.115490.

[35] B. Yeşilata, M. Bayram, A. Ustaoğlu, B. Kurşuncu, G. Hekimoğlu, A. Sarı, İ. Ü. Çıkman, O. Gencel, T. Ozbakkaloglu, Effects of cavity-shapes in 3D printed PCM encapsulation plates on sustainable thermal energy efficiency in buildings, Therm. Sci. Eng. Prog. 62 (2025) 103570, https://doi.org/10.1016/j.tsep.2025.103570.

[36] T.B. Freeman, K.E.O. Foster, K.B. Morgan, I. Melendez, A. Odukomaiya, S.K. S. Boetcher, Fused filament fabrication of thermoplastic polyurethane composites with microencapsulated phase-change material, Prog. Addit. Manuf. 22 (1) (2025), https://doi.org/10.1007/s40964-025-01277-0.

[37] G. Zhu, J. Wang, W. Luo, W. Chen, Y. Ma, X. Jiang, Q. Li, X. Hu, Solid-solid phase change films with intrinsic flexibility and photo-thermal conversion capabilities for human thermal management, Sol. Energy Mater. Sol. Cells 298 (2026) 114158, https://doi.org/10.1016/j.solmat.2025.114158.

[38] P. Manoj Kumar, K. Mylsamy, K. Alagar, K. Sudhakar, Investigations on an evacuated tube solar water heater using hybrid-nano based organic phase change material, Int. J. Green Energy, 17(13) (2020) 872-883 doi: 10.1080/15435075.2020.1809426.

[39] P.T. Saravanakumar, S.P. Arunkumar, B. Brailson Mansingh, P. Manoj Kumar, R. Subbiah, V.K. Eswarlal, Investigating the effect of thermal cycling on thermal characteristics of the nano-silica based phase changing material (PCM), Mater. Today: Proc., 50 (2022) 1502-1507 doi: 10.1016/j.matpr.2021.09.095.

[40] V.J. Reddy, M.F. Ghazali, S. Kumarasamy, Advancements in phase change materials for energy-efficient building construction: a comprehensive review, J. Storage Mater. 81 (2024) 110494, https://doi.org/10.1016/j.est.2024.110494.

[41] H. Togun, A. Basem, M.J. Jweeg, H.I. Mohammed, A.M. Abed, A.E. Anqi, A. Chattopadhyay, N. Biswas, Development and innovation using PCM in PV cooling systems: passive and active approaches, J. Therm. Anal. Calorim. 150 (2025) 10725–10760, https://doi.org/10.1007/s10973-025-14388-1.

[42] E. Passaglia, S. Coiai, G. Giordani, E. Taburoni, L. Fambri, V. Pagani, M. Penco, Modulated crosslinking of polyolefins through radical processes in the melt, Macromol. Mater. Eng. 289 (9) (2004) 809–817, https://doi.org/10.1002/mame.200400155.

[43] J. Kolařík, Z. Kruliš, M. Šlouf, L. Fambri, High-density polyethylene/cycloolefin copolymer blends. Part 1: phase structure, dynamic mechanical, tensile, and impact properties, Polym. Eng. Sci., 45(6) (2005) 817-826 doi: 10.1002/pen.20337.

[44] S. Bahlouli, A. Belaadi, A. Makhlouf, H. Alshahrani, M.K.A. Khan, M. Jawaid, Effect of fiber loading on thermal properties of cellulosic washingtonia reinforced HDPE biocomposites, Polymers 15 (13) (2023), https://doi.org/10.3390/polym15132910.

[45] R. Salgado-Pizarro, G. Ulldemolins, M.E. Navarro, A. Palacios, A. Calderón, Y. Ding, A.I. Fernández, C. Barreneche, New shape-stabilized phase change materials obtained by single-screw extruder, Energy Storage 3 (6) (2021) e268.

[46] S. Sacchet, G.P. Lolato, F. Valentini, M. Grigiante, L. Fambri, Thermophysical properties of high density polyethylene and phase change materials: a systematic study in the evaluation of specific heat capacity and thermal diffusivity, J. Therm. Anal. Calorim., (2025 - submitted) doi:.